Three-dimensional DC Resistivity Modeling using Galerkin Finite Element Method Composed by Tetrahedral Elements

4 authors, including:

Wahyu Srigutomo
Bandung Institute of Technology
149 PUBLICATIONS   271 CITATIONS

SEE PROFILE

Eleonora Agustine
Universitas Padjadjaran
37 PUBLICATIONS   41 CITATIONS

SEE PROFILE

Harry Mahardika
Bandung Institute of Technology
17 PUBLICATIONS   165 CITATIONS

SEE PROFILE

Some of the authors of this publication are also working on these related projects:

Modeling and Inversion Lab. View project

Environmental View project

Three-dimensional DC Resistivity Modeling using Galerkin Finite Element Method Composed by Tetrahedral Elements

Wahyu Srigutomo[1]*, Hairil Anwar[1], Eleonora Agustine[2] & Harry Mahardika[1]

[1]Physics of Earth and Complex System, Physics Department, Faculty of Mathematics and Natural Sciences, Institut Teknologi Bandung, Jalan Ganesha No. 10, Bandung 40132, Indonesia
[2]Geophysics Department, Faculty of Mathematics and Natural Sciences, Universitas Padjadjaran, Jalan Raya Bandung-Sumedang Km. 21, Jatinangor, Sumedang 45363, Indonesia
*E-mail: wahyu@fi.itb.ac.id

Abstract. Successful interpretation of DC resistivity data depends on the availability of a proper forward modeling scheme. In this study, a three-dimensional DC resistivity forward modeling scheme was developed using the finite element method. The finite element equations were obtained using a weakened form of the weighted-residual method called the Galerkin method. Discretization of the modeling domain was carried out by dividing it into smaller three-dimensional blocks and subdividing each block into five tetrahedral elements. A linear interpolation function was employed and elemental linear equations were set up, followed by formation of global matrix systems of equation and incorporation of proper boundary conditions. The conjugate gradient method was applied to solve the global system of equations, which in this study was proven to be more efficient than a direct solver, contributing to a 67% time reduction. Using a Wenner array configuration, comparison with theoretical calculation of the electric potential for a homogeneous model yielded a relative error of 3.66%. To confirm the applicability of this forward modeling scheme, apparent resistivity profiles for several basic three-dimensional subsurface resistivity models were compared with the analytical profiles, yielding an acceptable level of fitting.

Keywords: *apparent resistivity; conjugate gradient method; forward modeling; Galerkin finite element; Wenner configuration.*

1   Introduction

Numerical modeling involving calculation of electric fields based on the resistivity structure of the modeling domain can be grouped into two major techniques: the integral equation (IE) method and differential equation methods. The IE method was pioneered by Dieter, *et al.* [1] and further developed by Okabe [2], who introduced the boundary element method as a variant of the integral equation method. Later, the boundary element method was applied by

Xu [3] and Furman, *et al.* [4] for a modeling domain that can be divided into a relatively small number of subdomains. The IE method ensures higher computation speed and requires less computer memory since it only considers accumulation of charges at the interface of different resistivities. However, it is only effective for models that have limited inhomogeneities. Thus, to tackle model computation with more inhomogeneities, differential equation methods are used. Generally, the differential equations methods are grouped into two major divisions: finite difference (FD) and finite element (FE) methods. In these methods the modeling domain is discretized into smaller subdomains, cells or elements. The solutions of the modeling scheme in the entire domain are sought by solving a linear system of equations after manipulating the associated partial differential equation and its appropriate boundary conditions. Mufti [5] applied the FD method for modeling a 2D resistivity structure and Dey & Morrison [6] extended the FD analysis for modeling a 3D environment. Improvement for more accurate electric potential calculation by introducing more appropriate boundary conditions was presented by Zhang, *et al.* [7]. The FE method in electromagnetic and electrical modeling was first introduced by Coggon [8], who showed its suitability for modeling irregularly shaped 2D structures with varying physical properties. The FE analysis for 3D resistivity modeling was discussed for example by Pridmore, *et al.* [9], Sasaki [10], Li & Spitzer [11], and Rucker, *et al.* [12].

In this paper, we discuss the implementation of the Galerkin approach of the FE method, which is grouped into a family of weighted residual methods. In these methods, the solution is searched by weighting the residual of the governing differential equation [13]. The 3D modeling domain is divided into several blocks. These blocks are then subdivided into five tetrahedral elements. A linear interpolation function is selected to provide an approximation of the unknown solution of an element, followed by arrangement of the system of equations using the Galerkin method. The conjugate gradient method (CGM) was employed to solve the system of equations as an alternative to direct solver based on Gauss-Jordan elimination or LU decomposition [13]. To check the applicability of this modeling scheme, the apparent resistivity of the Wenner configuration was calculated based on the geometric factor obtained from the FEM solution for a known subsurface resistivity distribution and for a constant electric current that is injected into the ground.

2   Direct Current (DC) Resistivity Method: Wenner Array

The theoretical concept of the DC resistivity method is based on Poisson's equation for electrical problems,

$$\nabla.(\sigma\nabla V) = -I\delta(x - x_O)\delta(y - y_O)\delta(z - z_O) \tag{1}$$

where V is the electric potential (V), σ is the electrical conductivity of the medium (Sm^{-1}), which is the inverse of electrical resistivity ρ (Ωm), and I is the injected current (A) at coordinate (x_o, y_o, z_o). The above equation can be derived from Ohm's law, the relation between the electric field and the potential, and the continuity equation for electric charges. For a homogeneous earth, at all locations other than the location of the injected current, the right-hand side of Eq. (1) is equal to zero and the equation turns into an expression of Laplace's equation for V. The solution for Laplace's equation is given by [e.g. 14,15]

$$V = \frac{I\rho}{2\pi r},\tag{2}$$

where r is the distance from the observation point to the current source.

In the so-called Wenner array, the measured electric potential at the surface is the potential difference between two positions of electrodes at the surface due to the presence of a current source and a current sink. The array has a symmetrical setup about the center for both current and potential electrodes. The distance between the potential electrodes (P1-P2) is a and the distance between the current source and the current sink (C1-C2) is 3a. The configuration of the Wenner array is illustrated in Figure 1. Using Eq. (2) for this configuration, the measured electric potential difference is given by:

$$\Delta V = \frac{I\rho}{2\pi}\left[\left(\frac{1}{r_1} - \frac{1}{r_2}\right) - \left(\frac{1}{r_3} - \frac{1}{r_4}\right)\right] = \frac{I\rho}{2\pi a} = \frac{I\rho}{K},\tag{3}$$

where $K = 2\pi a$ is defined as the geometric factor of the Wenner array. Once we know the injected current and the measured potential difference for a certain K, we can calculate the resistivity of the homogeneous medium easily, as shown by the right-hand side of Eq. (3). If the medium is inhomogeneous, the calculated resistivity is no longer the true resistivity, but becomes what is called the apparent resistivity,

$$\rho_{app} = K\frac{\Delta V}{I}.\tag{4}$$

The apparent resistivity is the measured resistivity between two potential electrodes for a certain value of K and for a recorded ΔV as if it were caused by a homogeneous subsurface. In real geophysical applications, the apparent resistivities for different values of K shown in Eq. (4) are numerically processed simultaneously to obtain information on the true resistivity profile below the surface.
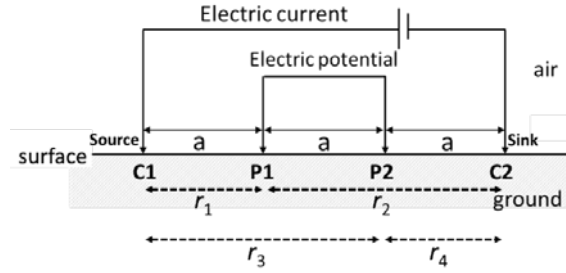
Figure 1 Wenner configuration of current and potential electrodes for measuring subsurface resistivity. C1 and C2 denote the positions of the current source and current sink at the surface, respectively. P1 and P2 represent the positions of the potential electrodes for potential difference measurement, while r and its subscripts represent the distances between the current-potential electrodes.

3   Galerkin Finite Element Method with Tetrahedral Mesh

The finite element method (FEM) is a numerical solution for solving partial differential equations (PDE) constrained by boundary and initial conditions. In FEM the modeling domain is divided into smaller sub-domains called elements. The computed primary quantity distribution, whose value is unknown inside the elements, is interpolated from values at each node of the elements. The interpolating function must be a complete set of polynomials where the accuracy of FEM's solution depends on the chosen polynomial order.

In this study, we applied the Galerkin approach to the FEM analysis for the 3D DC resistivity modeling problem. From the perspective of the weighted residual method, all terms of the second-order PDE under study are transferred to the right-hand side of the equation, leaving a residual on the left-hand side. This residual is multiplied by a weight function and integrated over the domain of the element [16]. The weight function and its associated interpolation function must be twice differentiable. To soften this requirement a weak formulation is implemented by using partial integration and disseminating the second derivative equivalently between the weight function and the interpolation function in such a way that both functions are only once differentiable.

The second-order partial differential equation for a 3D domain in a Cartesian coordinate system can be written as follows [17]:

$$\frac{\partial}{\partial x}\left(\alpha_x \frac{\partial u}{\partial x}\right) + \frac{\partial}{\partial y}\left(\alpha_y \frac{\partial u}{\partial y}\right) + \frac{\partial}{\partial z}\left(\alpha_z \frac{\partial u}{\partial z}\right) = g, \tag{5}$$

where αx, αy, αz and g are constants and u represent the unknown primary quantity.

Looking at the relation between the electric potential and the current in Eq. (1), we have $u = V$, $\alpha_x = \alpha_y = \alpha_z = \sigma$, and $g = -I\delta(x - x_o)\delta(y - y_o)\delta(z - z_o)$ for our modeling problem.

3.1   Domain Discretization

In a 2D environment, domain discretization with rectangular elements will not always fit a complex domain and the number of geometrical errors produced from rectangular element discretization is quite significant. One way to fix this is by using smaller rectangular elements, which will consume more computational time and leads to an enormous number of elements inside the domain.

An effective way for reducing the number of geometrical errors is by using triangular and quadrilateral elements instead of rectangular elements. This produces a better fit with a complex modeling domain than using rectangular elements.

A 3D domain is bounded by a closed surface. The simplest non-rectangular discretization of the domain elements for a 3D domain that is still suitable for a more complex geometry consists of four-node tetrahedral elements. Implementation of tetrahedral elements in 3D geoelectric FEM modeling has been carried out previously by several authors, e.g. Blome, *et al.* [18], Rucker, *et al.* [12], Gunther, *et al.* [19] and Song, *et al.* [20]. In our study, the earth was modeled by a large rectangular body that was divided into smaller rectangular blocks. Each block was divided again into five tetrahedral prisms or elements (Figure 2).

Each node or corner of these prisms was attached to four nodes of the rectangular block. The above discretization steps yield a structured mesh system. One of the important steps in the FEM discretization scheme is the connectivity setup between the local and global coordinates of the elements that will determine the shape and size of the global matrix system to be solved.

3.2   Interpolation Function and Weighted Residual Method

The chosen interpolation function must guarantee that the unknown values of the primary quantity to be solved are continuous inside the modeling domain. This function also must be in polynomial form, which means it should be

differentiable at least once. The unknown values inside the elements can be obtained from interpolating the values of the elemental nodes such that [13,16]

$$u = \sum_j u_j^e N_j \tag{6}$$

where u is a value inside an element, u_j are the values on the element nodes, N_j is the interpolation function of each node. A tetrahedral element in the Cartesian (x-y-z) coordinate system can be mapped onto a local system coordinate called the natural (ξ-η-ζ) coordinate system as shown in Figure 2. This local coordinate system allows us to specify any point inside an element with a set of non-dimensional numbers whose value remains between 0 and 1.
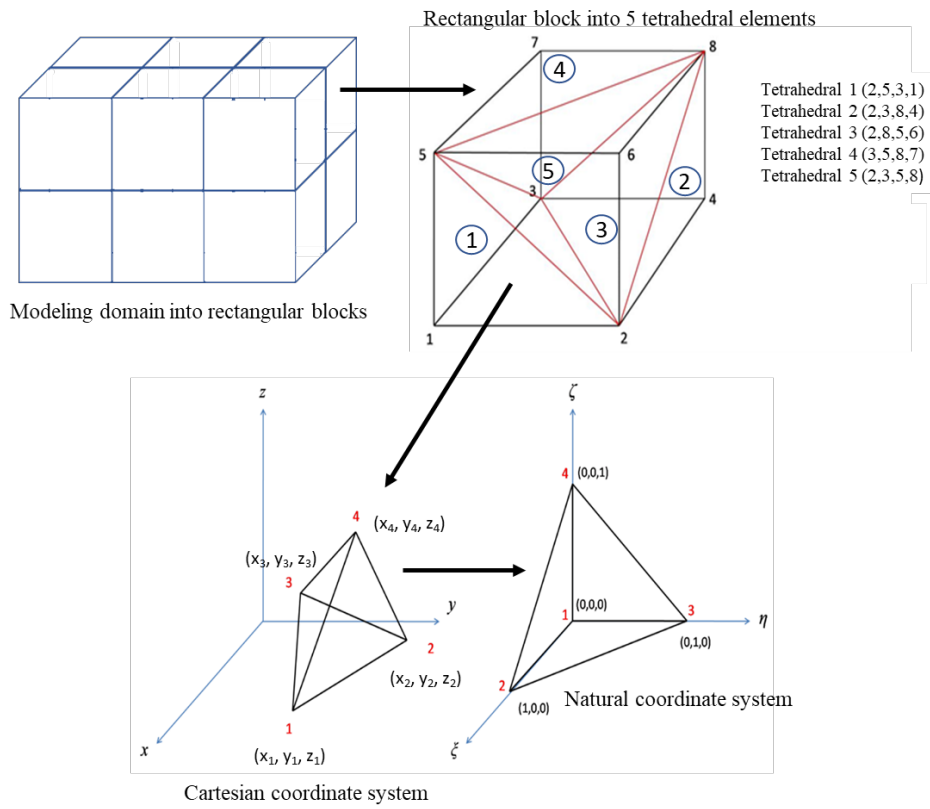
Figure 2 Division of the modeling domain into rectangular blocks and the blocks into tetrahedral elements with the connectivity between an element and the nodes of its associated block (upper). Illustration of elemental coordinate transformation from the Cartesian coordinate system into the natural coordinate system (lower).

In our cases, a tetrahedral element has four interpolation functions, i.e. $N_1(\xi, \eta, \zeta)$, $N_2(\xi, \eta, \zeta)$, $N_3(\xi, \eta, \zeta)$, and $N_4(\xi, \eta, \zeta)$. Interpolation function $N_1(\xi, \eta, \zeta)$ is the interpolation function for node 1 of the tetrahedral element, where $N_1(\xi, \eta, \zeta)$ is equal to 1 at node 1 and equals to 0 for the other nodes. The rule for $N_1(\xi, \eta, \zeta)$ is also applied to $N_2(\xi, \eta, \zeta)$, $N_3(\xi, \eta, \zeta)$, and $N_4(\xi, \eta, \zeta)$, such that the general interpolation function for a tetrahedral element can be written as:

$$N_j\left(\xi,\eta,\zeta\right)= a_j + b_j\xi + c_j\eta + d_j\zeta, \tag{7}$$

which in this case is linear and a_j, b_j, c_j, d_j are constants that should be determined for $N = 1, 2, 3$, and 4.

The implementation of the weighted residual method begins with arrangement of element residual r^e, which is formed by moving the right-hand side of Eq. (8) to the left. This residual is then multiplied by a weight function w and integrated over the volume of the element. The value of this integration is equal to zero and therefore:

$$\int_{\Omega^e} w\left[\frac{\partial}{\partial x}\left(\alpha_x\frac{\partial u}{\partial x}\right)+\frac{\partial}{\partial y}\left(\alpha_y\frac{\partial u}{\partial y}\right)+\frac{\partial}{\partial z}\left(\alpha_z\frac{\partial u}{\partial z}\right)-g\right]dxdydz = 0. \tag{8}$$

Consecutively, by applying the partial differential identity, the divergence theorem, substitution of Eq. (5) and applying Galerkin's approach of $w = N_i$ into Eq. (8) and expressing it in matrix form, we have the following expression [15]:

$$\begin{bmatrix} K_{11}^e & K_{12}^e & \cdots & K_{1n}^e \\ K_{21}^e & K_{22}^e & \cdots & K_{2n}^e \\ \vdots & \vdots & \ddots & \vdots \\ K_{n1}^e & K_{n2}^e & \cdots & K_{nn}^e \end{bmatrix} \begin{Bmatrix} u_1^e \\ u_2^e \\ \vdots \\ u_n^e \end{Bmatrix} = \begin{Bmatrix} f_1^e \\ f_2^e \\ \vdots \\ f_n^e \end{Bmatrix} + \begin{Bmatrix} p_1^e \\ p_2^e \\ \vdots \\ p_n^e \end{Bmatrix}. \tag{9}$$

Each element in the above **K** matrix can be calculated as:

$$K_{ij}^e = \frac{|\mathbf{J}|}{6}\left[\alpha_x\frac{\partial N_i}{\partial x}\frac{\partial N_j}{\partial x}+\alpha_y\frac{\partial N_i}{\partial y}\frac{\partial N_j}{\partial y}+\alpha_y\frac{\partial N_i}{\partial z}\frac{\partial N_j}{\partial z}\right]. \tag{10}$$

J in Eq. (10) is a matrix given by:

$$\mathbf{J} = \begin{pmatrix} \overline{x}_{21} & \overline{y}_{21} & \overline{z}_{21} \\ \overline{x}_{31} & \overline{y}_{31} & \overline{z}_{31} \\ \overline{x}_{41} & \overline{y}_{41} & \overline{z}_{41} \end{pmatrix}, \tag{11}$$

where $\bar{x}_{ij} = x_i - x_j$. The value of x, y, and z inside a tetrahedral element can be obtained by interpolating the value of x, y, and z of the nodes in that element. From Eq. (6), Eq. (7) and Eq. (11) the values of x, y, and z are:

$$x = x_1 + \bar{x}_{21}\xi + \bar{x}_{31}\eta + \bar{x}_{41}\zeta$$
$$y = y_1 + \bar{y}_{21}\xi + \bar{y}_{31}\eta + \bar{y}_{41}\zeta \qquad (12)$$
$$z = z_1 + \bar{z}_{21}\xi + \bar{z}_{31}\eta + \bar{z}_{41}\zeta$$

The elements of vector $\mathbf{f}$ in Eq. (9) are obtained by solving the following integration:

$$f_i^e = \iiint_{\Omega^e} N_i I \delta(x - x_o) \delta(y - y_o) \delta(z - z_o) dx dy dz, \qquad (13)$$

which includes x, y, and z expressed previously by Eq. (12).

Vector $\mathbf{p}$ in Eq. (9) only needs to be solved at the modeling domain boundaries, which has either a Neumann or a mixed boundary condition and is expressed as:

$$p_i^e = \iint_{\Gamma^e} q N_i dS - \iint_{\Gamma^e} \gamma N_i \left(N_1 u_1^e + N_2 u_2^e + N_3 u_3^e + N_4 u_4^e \right) dS, \qquad (14)$$

where dS is the area of the domain boundary, and q and γ are the source and parameter of the mixed boundary condition. In order to get a proper solution of the problem involving Eq. (13) and Eq. (14) we need to apply the boundary condition for each side of the modeling domain. On the upper side of the domain we apply a Neumann boundary condition, written as:

$$\left. \frac{\partial V}{\partial n} \right|_\Gamma = 0. \qquad (15)$$

We assume that there is no current flowing over the upper side of the modeling domain, which is in coincidence with the surface, due to the large value of air resistivity, ensuring the validity of Eq. (15). On the other hand, we apply a Dirichlet boundary condition for the rest of the domain boundaries, considering a condition for the electric potentials, which tend to be zero at long distances from the source. The Dirichlet boundary condition is written as:

$$\left. V \right|_\Gamma = 0. \qquad (16)$$

Therefore, to ensure that Eq. (16) is satisfied, the dimensions of the rectangular blocks near the boundaries were kept larger so as to make larger distances from the current source (Figure 3).

3.3   Global Matrix System

The elemental matrix equation (Eq. (9)) was then assembled to form a global matrix system

$$\mathbf{K} = \sum_e \mathbf{K}^e \tag{17}$$

and $$\mathbf{b} = \sum_e \mathbf{b}^e \tag{18}$$

where **b** was constructed from the source term in Eq. (13).

The matrix obtained at this step was still singular thus could not be run to produce a unique solution. To be able to give a unique solution, the Dirichlet boundary condition had to be imposed to the system of equations to make it non-singular:

$$\mathbf{K}'\mathbf{u} = \mathbf{b}', \tag{19}$$

where **K**' and **b**' are the **K** and **b** matrices in Eq. (17) and Eq. (18) respectively after the incorporation of the Dirichlet boundary condition. Application of Neumann and mixed boundary conditions was done by calculating vector **p** on Eq. (14) before the application of the Dirichlet boundary condition.

3.4   Solving the Global Matrix System

After all boundary conditions were properly installed into the global matrix system, the next step was to find a unique solution of Eq. (19) such that

$$\mathbf{u} = \left(\mathbf{K}'\right)^{-1}\mathbf{b}' \tag{20}$$

with $(\mathbf{K}')^{-1}$ is the inverse of matrix **K**'. Solving the system of equations expressed in Eq. (20) is the most expensive computation part in FEM. In this study we applied the conjugate gradient method (CGM), which belongs to the family of iterative methods and is highly efficient for solving large and sparse systems [21]. An exact solution is produced by CGM if the number of iterations equals the number of equations [13]. Furthermore, CGM may result in a practically accurate solution in sufficiently fewer iterations than the number of equations [22]. However, in this study comparison of computation time with the LU (lower-upper) decomposition method, which belongs to the family of direct solver methods, was carried out; the results will be discussed briefly in the next section.

Omitting the prime symbol (') in Eq. (19) and transforming it into a self-adjoint and positive definite problem by multiplying it with adjoint matrix $\mathbf{K}^a$ or $\mathbf{K}^a\mathbf{K}\mathbf{u} = \mathbf{K}^a\mathbf{b}$. Letting $\mathbf{B} = \mathbf{K}^a\mathbf{K}$ and $\mathbf{h} = \mathbf{K}^a\mathbf{B}$, Eq. [19] can be written as in Eq. (21):

$$\mathbf{B}\mathbf{u} = \mathbf{h}. \tag{21}$$

Adopting Jin [13] and Holmes [22] for the CGM algorithm, first an initial guest $\mathbf{u}_1$ was set up and the following computational procedure was conducted in Eq. (22):

$$\mathbf{r}_1 = \mathbf{h} - \mathbf{B}\mathbf{u}_1, \tag{22}$$

$$\mathbf{p}_1 = \mathbf{r}_1$$

In Eq. (23) perform iteration for $i = 1, 2, 3, \ldots, n$:

$$\alpha_i = \frac{\langle \mathbf{r}_i, \mathbf{r}_i \rangle}{\langle \mathbf{B}\mathbf{p}_i, \mathbf{p}_i \rangle}$$

$$\mathbf{u}_{i+1} = \mathbf{u}_i + \alpha_i \mathbf{p}_i$$

$$\mathbf{r}_{i+1} = \mathbf{r}_i - \alpha_i \mathbf{B}\mathbf{p}_i$$

$$\gamma_i = \frac{\langle \mathbf{r}_{i+1}, \mathbf{r}_{i+1} \rangle}{\langle \mathbf{r}_i, \mathbf{r}_i \rangle}$$

$$\mathbf{p}_{i+1} = \mathbf{r}_{i+1} + \gamma_i \mathbf{p}_i \tag{23}$$

As in Eq. (24) terminate when

$$\frac{\|\mathbf{r}_{i+1}\|}{\|\mathbf{h}\|} < \varepsilon, \tag{24}$$

where ε is the tolerance or the desired accuracy of solution. The angle brackets in the above algorithm denote the inner product between the vectors inside it.

4   Results and Discussion

The forward modeling was realized by a large rectangular earth whose dimensions were LX x LY x LX = 270 m x 240 m x 150 m. There were 42 x 36 x 24 smaller rectangular blocks generated from the discretization of the modeling domain. Each of these blocks comprised of five tetrahedral elements, making up a total number of elements equal to 181440. As previously mentioned, the

dimensions of the blocks were made larger near the modeling boundaries where the Dirichlet boundary condition was applied (Figure 3).

4.1 Homogeneous Model

The functionality of the modeling scheme was tested by first calculating the responses from a homogeneous earth of 100 Ωm. Two constant electric currents with values of 1 A and -1 A were injected at C1 and C2, respectively. The value of *a* was 5 and can be enlarged according to the principle of the Wenner array (Figure 3). Using Eq. (1) the electric potential was computed at each node of the 181440 elements. The resulted 3D potential distributions are shown in Figures 3 and 4. High positive and negative potential values concentrate around both the positive and the negative current electrodes respectively, as dictated by the theory. For the sake of clarity of the current flow directions, the computed current magnitude at each position was normalized by their own values, yielding a uniform length of currents. The normalized current flows beneath the surface are denoted by a set of arrows with different directions at all positions. The currents diverge out of the positive current electrode and converge towards the negative current electrode. Two symmetrical lobes of electric potential, each with positive and negative sign, are observed around the current electrode.

A comparison between the electric potential values resulted from the FEM scheme and the potential values calculated by analytical formulation along line A-B containing points C1, C1, P1 and P2, is shown in Figure 4b. The FEM potential values over the 100 Ωm homogeneous resistivity are close to the values resulted from the analytical calculation (Figure 4b). Noticeable discrepancies are observed exactly at the positions of the current electrodes. This is due to the singularities at the electrodes as represented by the δ-function on the right-hand side of Eq. (1), where the potential varies swiftly. However, in real geoelectric measurements we never simultaneously measure the potential difference between two exact positions of current electrodes. Although beyond our current study, it is worth mentioning that Lowry, *et al.* [23], Zhao & Yedlin [24], and Blome, *et al.* [18] proposed improvements in electric potential modeling accuracy in the vicinity of current electrodes by applying the so called singularity removal. This was carried out by splitting the electric potential into its singular or primary part resulted from a homogeneous half-space and non-singular or secondary part resulted by the difference between the real conductivity and the homogeneous conductivity.

The accuracy of this modeling scheme was tested by comparing the potential differences computed by this FEM scheme with those calculated analytically by using Eq. (2). The magnitude of the injected current was kept constant at $I = 1$ A and the value of *a* for the Wenner array was varied by setting its value to 5,

10, 15, 20, 25, and 30 m. The computed electric potential differences are listed in Table 1.
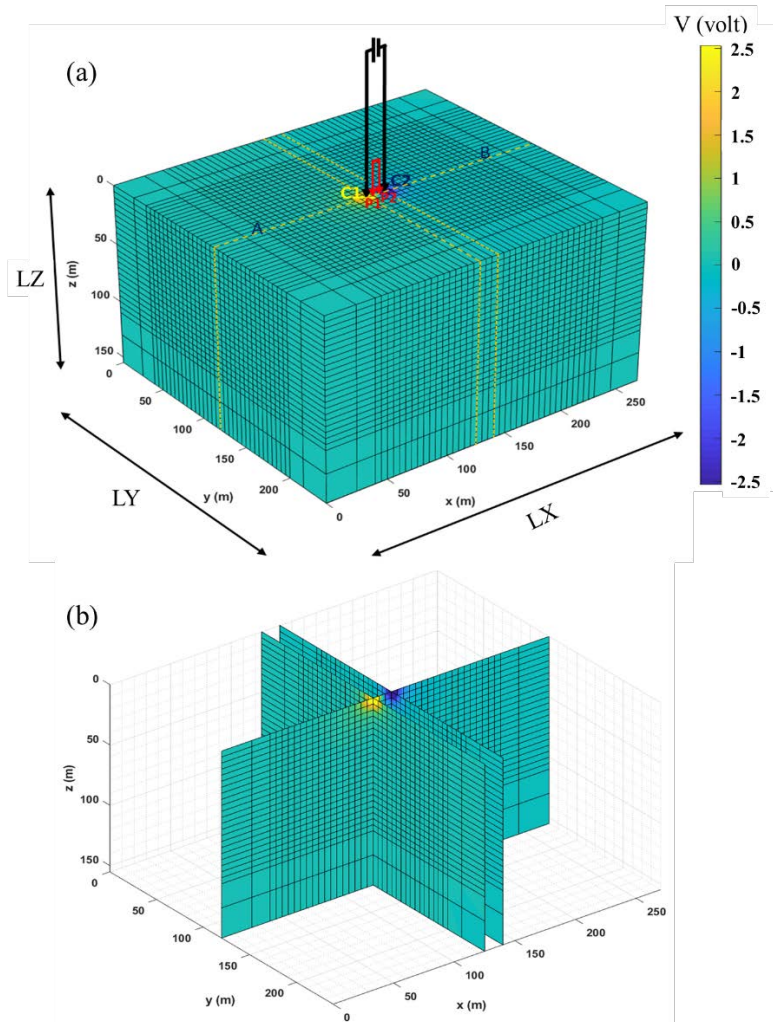
Figure 3 (a) Modeling domain discretization into rectangular blocks comprising tetrahedral elements. The outer rectangular blocks have larger sizes to ensure the validity of the Dirichlet boundary condition that is used at all the sides of the domain, except at the surface. C1 and C2 denote the positions of the current electrodes, while P1 and P2 represent the positions of the potential electrodes, respectively, illustrating a Wenner array. An electric current of 1 A was injected into a homogeneous earth of 100 Ωm; the electric potential was calculated in volt within the domain. (b) Examples of vertical sections of potential calculated by this FEM scheme.
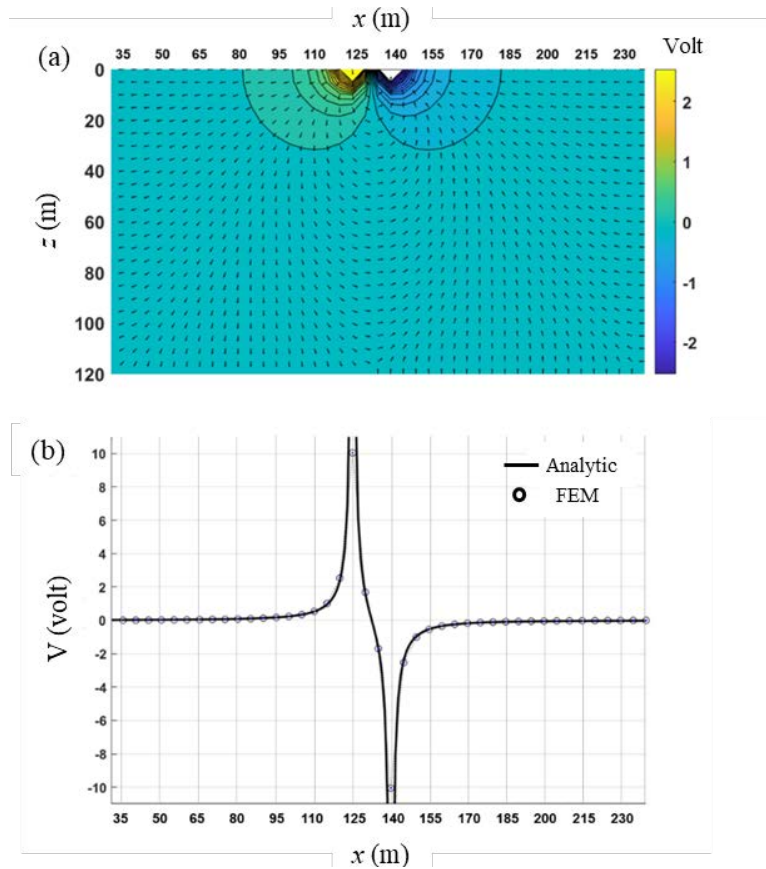
Figure 4 (a) Detailed vertical section of the electric potential distribution and normalized current flow directions within the subsurface for a 100 Ωm homogeneous earth along line A-B in Figure 3a. The value of *a* is 5 m and C1 and C2 is located at 125 m and 140 m respectively. (b) Comparison between the electric potential profile resulted from the FEM scheme and the analytical potential profile for *a* = 5 m at the surface along line A-B in Figure 3a.

As shown by Table 1, the discrepancies between the potential differences that were computed by FEM and those calculated by the analytical expression for different values of *a* gave an average relative error of 3.66%. Most of the contribution to this error came from the surface potentials very close to the singularity points (< 1 m) as shown in Pan & Tang [25], where the relative error may exceed 10% for FEM modeling scheme without singularity removal similar to our scheme.

Within the scope of this modeling scheme, based on the known homogeneous resistivity, the injected currents and the computed potential differences for

varying values of a, we found that the geometrical factor for the Wenner array, K, consistently equals $5.917a$ as can be seen in Table 1. The value of K is below its theoretical value, which should be $2\pi a$. The discrepancy of the computed and the theoretical K is caused by the error in the computed potential difference as shown before. Therefore, for other cases of an inhomogeneous subsurface resistivity distribution where the apparent resistivity value for a particular value of a is sought, $K = 5.917a$ was used to ensure that the calculated apparent resistivity remains as close as possible to its true resistivity distribution.

Table 1   Results of FEM modeling for a homogeneous earth of 100 Ωm and injected current of 1 A.

| a (m)	ΔV analytic (volt)	ΔV FEM LU	ΔV FEM CGM	% Error ΔV LU	% Error ΔV CGM	K/a LU	K/a CGM	Time (s) LU	Time (s) CGM
5	3.1847	3.3736	3.3736	5.93	5.93	5.917	5.917	174.16	99.81
10	1.5924	1.6968	1.6968	6.56	6.56	5.917	5.917	195.04	57.73
15	1.0616	1.0830	1.0830	2.02	2.02	5.917	5.917	219.06	70.36
20	0.7962	0.7934	0.7934	0.35	0.35	5.917	5.917	234.13	58.77
25	0.6369	0.6220	0.6220	2.35	2.35	5.917	5.917	163.60	71.01
30	0.5308	0.5054	0.5054	4.78	4.78	5.917	5.917	199.63	57.66
			average	**3.66**	**3.66**			**197.60**	**69.22**

One of crucial steps in FEM is solving the linear system of equations, particularly consideration accuracy and time consumption. As stated above, usually direct solver approaches (e.g. Gaussian elimination, LU, Cholesky, and QR decomposition) are deemed to generate exact solutions at the expense of computational time. Therefore, in this study, CGM was applied to meet the requirement of having equally accurate solutions as those of the direct method with significant reduction of computation time. A comparison of time to solve the system of linear equations in this 3D FEM modeling between LU decomposition and CGM is listed in Table 1. The computation time needed to solve the system of equations was always shorter for CGM compared to that of LU decomposition for exactly the same solutions. The time required by CGM was 2.85 times shorter or about 65% more efficient than the time required by LU decomposition when dealing with 181440 tetrahedral elements. The computation was performed on a personal computer with Intel Core i7-7700T CPU @ 2.90 GHz, 16.384 GB RAM.

4.2   Inhomogeneous Models

Comparison between the computed apparent resistivity – based on potential difference – resulted from this FEM modeling scheme and the calculated apparent resistivity – based on its analytical expression – was performed for several simple models. Analytical expressions for simple models such as

layered earth and vertical contact can be found readily, for example in Telford, *et al.* [15] and Bhattacharya & Shalivahan [14]. The expressions involve the utilization of the modified Bessel function of the first kind of order 0 and 1.

The first inhomogeneous model to be compared was a two-layered model comprising a conductive top layer $\rho_1 = 10$ Ωm whose thickness $d = 15$ m, and a resistive bottom half-space $\rho_2 = 100$ Ωm. Potential distribution and current flow directions below the surface are shown in Figure 5a for a line on which C1, C2, P1 and P2 are located. Following Ohm's law, the overall values of electric potential are low in a conductive medium. However, the current lines are concentrated within the conductive medium. The current lines tend to be channeled in the upper layer, where their direction is mostly horizontal, yielding almost vertical isopotential surfaces. The current lines are refracted toward the normal when crossing the interface and spread radially in the resistive medium, yielding radially concentric isopotential surfaces.
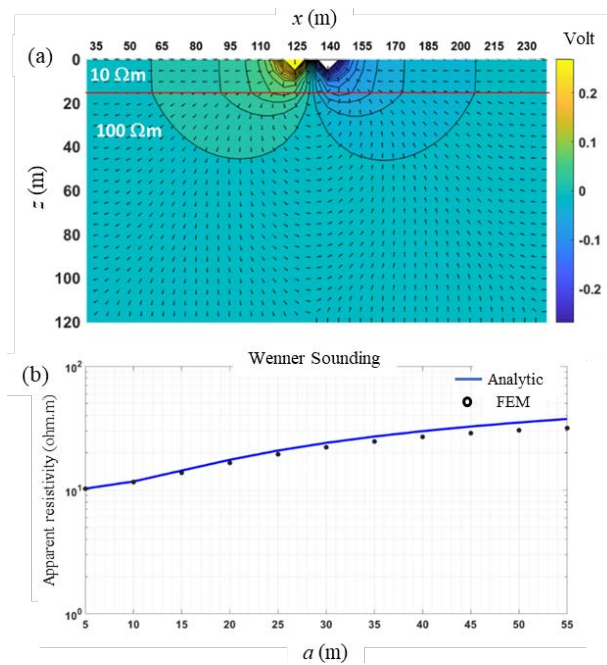
Figure 5 (a) Cross section of a two-layered model with top layer $\rho_1 = 10$ Ωm, thickness $d = 15$ m, and bottom half-space with $\rho_2 = 100$ Ωm. C1 and C2 are located at 125 and 140 m, respectively. Colors and arrows respectively depict the potential distribution and current flow directions. (b) Comparison between the FEM Wenner array sounding curve and the analytical curve; a was varied from 5 to 55 m.

The curves of the FEM and analytical apparent resistivities that would be recorded at the surface for a Wenner array sounding for the two-layered model in Figure 5(a) are shown in Figure 5(b). The value of a was varied from 5 to 55 m. The FEM curve adequately resembles the analytical curve. However, discrepancies between the two curves are larger at larger values of a, which may be attributed to the presence of coarser blocks of elements near the edges of the modeling domain.
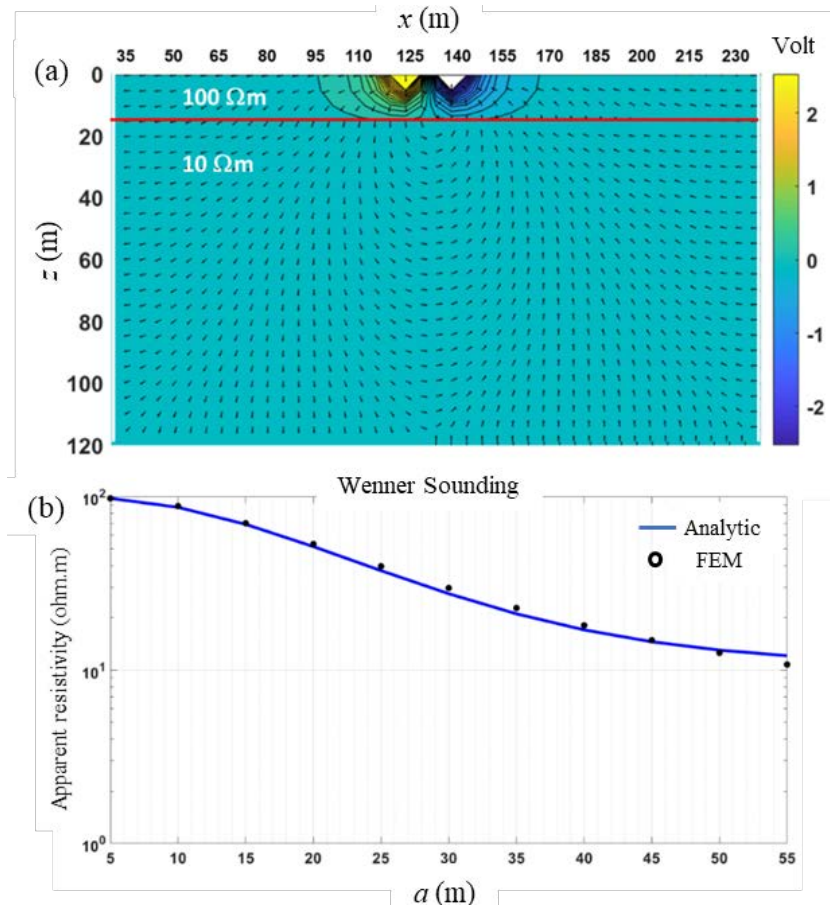

Figure 6 (a) Cross section of a two-layered model with top layer $\rho_1 = 100$ Ωm, thickness $d = 15$ m, and bottom half-space with $\rho_2 = 10$ Ωm. (b) Comparison between the FEM Wenner array sounding curve and the analytical curve; a was varied from 5 to 55 m.

Figure 6(a) depicts a two-layered model whose geometry is the same as the model in Figure 5(a), but the values of resistivity are interchanged. The resistivity of the top layer is $\rho_1 = 100$ Ωm with thickness $d = 15$ m and the

resistivity of the bottom half-space $\rho_2 = 10$ Ωm. The resistive top layer tends to diverge the current lines with radial patterns. A relatively high potential distribution is observed only at the top layer of this model. The current flows are refracted across the interface of the top layer and the bottom layer outward from the normal as dictated by the theory. A very good fitting between the FEM Wenner array sounding curve and the analytical curve of apparent resistivity is shown in Figure 6(b). A noticeable discrepancy between the two curves is observed for very large a (= 55 m), as also observed from Figure 5b. In this modeling scheme, errors contributed by the singularity at the positions of current source and sink have been corrected by considering the computed K (= 5.917a) listed in Table 1. However, a large discrepancy was still encountered for larger distances between current electrodes and potential electrodes. This feature may be attributed to the effects of the domain boundaries, size and number of the elements, or the selected interpolation function in the FEM formulation. Pan & Tang [25] also showed large relative errors between the analytical and FEM apparent resistivity curves for larger distances of current-potential electrode separation in a layered model (using a Schlumberger array) and for a vertical dyke model (using a pole-pole array).

The third model to be evaluated was a model with a vertical contact. In reality, a vertical contact may represent a vertical fault or one side of a wide vertical dyke. This model is depicted in Figure 7(a). In practice, investigating the presence of a vertical contact is carried out by applying a Wenner array profiling measurement. In this measurement, a is kept constant and the central point between P1 and P2 is shifted laterally at an equal distance. In this model, the vertical contact was located at $x = 165$ m separating a conductive region of 10 Ωm and a resistive region of 100 Ωm; a was set to 10 m and the measurement configuration was shifted at every 5 m from the conductive side toward the resistive side.

Figure 7(b) shows the plot of apparent resistivity versus position of Wenner array center point. The apparent resistivity profile exhibits a discontinued feature around the point of contact and shows the presence of cusps when one of the current electrodes was exactly on the vertical contact. Reynolds [26] explained that this feature of resistivity profile near a vertical contact is caused by the change in current density that affects the potential gradient at the potential electrodes. Figure 7(b) shows an acceptable fitting between FEM's apparent resistivity curve and the analytical curve.
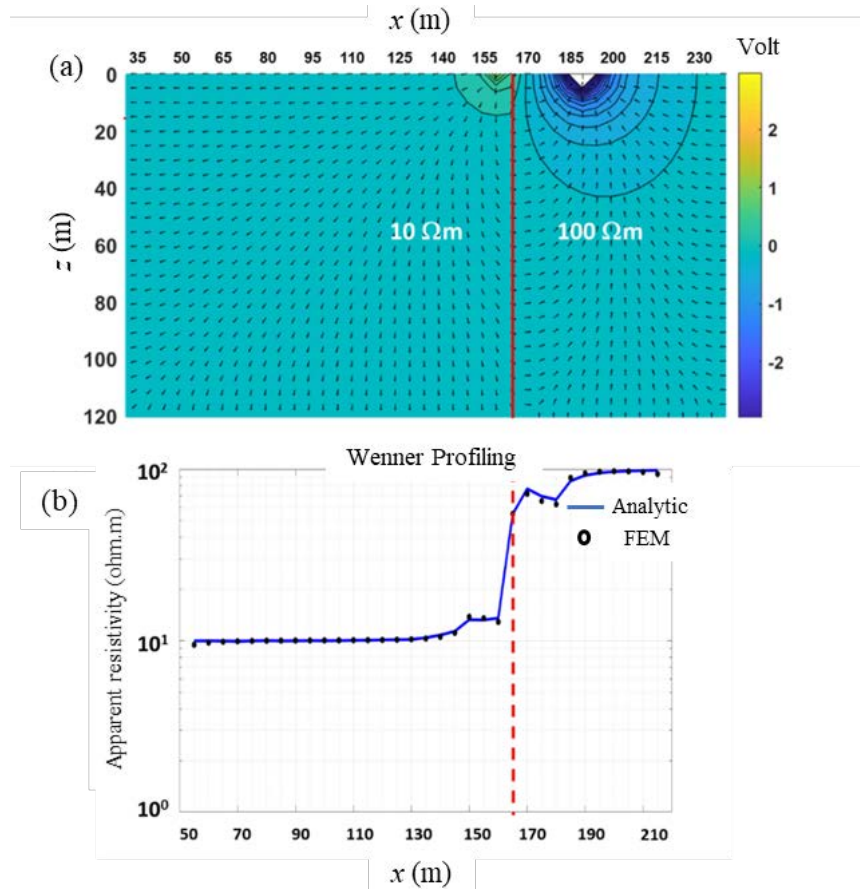
Figure 7 (a) Model of vertical contact at $x = 165$ m separating $\rho_1 = 10$ Ωm and $\rho_2 = 100$ Ωm; a was kept constant at 10 m and the measurement configuration was shifted at an equal distance of 5 m. (b) Comparison between FEM's apparent resistivity profile and the analytical profile.

5   Conclusions

We have developed a 3D DC resistivity modeling scheme using a weak formulation version of the weighted-residual finite element method called the Galerkin approach. The 3D modeling domain was discretized into rectangular blocks and these blocks were subdivided into five tetrahedral elements each. After imposing a Newmann boundary condition to the ground-air interface and a Dirichlet boundary condition to the other surfaces, the arranged global system of linear equations is solved iteratively using the conjugate gradient method (CGM). Compared to a direct solver, CGM reduced the required computational

time significantly, yielding a time reduction of 67% for a model with 181440 tetrahedral elements.

Applicability of the forward modeling scheme was tested by comparing the results for a Wenner configuration with those when using an analytical expression, yielding an overall relative error of 3.66%, which is still acceptable for practical use. The forward scheme was also employed to reveal the responses of layered-earth and vertical contact models in terms of realistic apparent resistivity profiles. Comparison between the FEM computed apparent resistivity profiles and the analytically calculated profiles confirmed the applicability of the scheme to be used in a further numerical interpretation of resistivity data such as inversion. Future improvement of the forward modeling scheme may still be needed to enhance its performance by incorporating the singularity removal procedure and applying an unstructured mesh system, which is more flexible for models with complex geometry.

Acknowledgements

References

[1]   Dieter, K., Paterson, N.R. & Grant, F.S., *IP and Resistivity Type Curves for Three-Dimensional Bodies*, Geophysics, **34**, pp. 615-632, 1969.

[2]   Okabe, M., *Boundary Element Method for the Arbitrary Inhomogeneities Problem in Electrical Prospecting*, Geophys. Prospect., **29**, pp. 39-59, 1981.

[3]   Xu, S.Z., *The Boundary Element Method in Geophysics*, Geophysical Monograph Series Number 9, SEG, 2001.

[4]   Furman, A., Warrick, A.W. & Ferré, T.P.A., *Electrical Potential Distributions in Response to Applied Current in a Heterogeneous Subsurface, Solution for Circular Inclusions*, Vadose Zone Journal, **1**(2), pp. 273-280, 2002.

[5]   Mufti, I.R., *Finite-Difference Resistivity Modeling for Arbitrarily Shaped Two-Dimensional Structures*, Geophysics, **41**, pp. 62-78, 1976.

[6]   Dey, A. & Morrison, H.F., *Resistivity Modeling for Arbitrarily Shaped Three-Dimensional Structures*, Geophysics, **44**(4), pp. 753-780, 1979.

[7]   Zhang, J., Mackie, R.L. & Madden, T.R., *3-D Resistivity Forward Modeling and Inversion Using Conjugate Gradients,* Geophysics, **60**(5), pp. 1313-1325, 1995.

[8]   Coggon, J.H., *Electromagnetic and Electrical Modeling by the Finite Element Method*, Geophysics, **36**(1), pp. 132-155, 1971.

[9]   Pridmore, D.F., Hohmann, G.W., Ward, S.H. & Sill, W.R., *An Investigation of Finite-Element Modelling for Electrical and Electromagnetical Data in Three Dimensions,* Geophysics, **46,** pp. 1009-1024, 1980.

[10] Sasaki, Y., *3-D Resistivity Inversion Using the Finite-Element Method, Geophysics,* **59**(12), pp. 1839-1848, 1994.

[11] Li, Y. & Spitzer, K., *Three-Dimensional DC Resistivity Forward Modelling Using Finite Elements in Comparison with Finite-difference Solutions*, Geophys. J. Int.*,* **151,** 924-934, 2002.

[12] Rucker, C., Gunther, T. & Spitzer, K., *Three-Dimensional Modelling and Inversion of Dc Resistivity Data Incorporating Topography I: Modelling*, Geophys. J. Int., **166**, pp. 495-505, 2006.

[13] Jin, J.M., *The Finite Element Method in Electromagnetics*, 3rd ed., John Wiley & Sons, Inc., 2014.

[14] Bhattacharya, B.B. & Shalivahan, *Geoelectric Methods Theory and Applications,* McGraw Hill Education (India) Private Limited, 2016.

[15] Telford, W.M., Geldart, L.P. & Sheriff, R.E., *Applied Geophysics*, Cambridge University Press, pp. 522-577, 1990.

[16] Polycarpou, A.C., *An Introduction to the Finite Element Method in Electromagnetism*, Morgan & Claypool, 2006.

[17] Reddy, J.N, *An Introduction to the Finite Element Method*, McGraw-Hill, 1993.

[18] Blome, M., Maurer, H.R. & Schmidt, K., *Advances in Three-Dimensional Geoelectric Forward Solver Techniques*, Geophysical Journal International*,* **176**(3), pp. 74-752, 2009.

[19] Gunther, T., Rucker, C. & Spitzer, K., *Three-Dimensional Modelling and Inversion of DC Resistivity Data Incorporating Topography – II: Inversion*, *Geophysical Journal International*, **166**(2), pp. 506-517, 2006.

[20] Song, T., Liu, Y. & Wang, Y.*, Finite Element Method for Modeling 3D Resistivity Sounding on Anisotropic Geoelectric Media*, Mathematical Problems in Engineering, Article ID 8027616, pp. 1-12, 2017.

[21] Spitzer, K. & Wurmstich, B., *Speed and Accuracy in 3D Resistivity Modeling,* in Three-Dimensional Electromagnetics, eds. Oristaglio, M. & Spies, B., no. 7 in Geophysical Developments, Society of Exploration Geophysicists, 1999.

[22] Holmes, M.H., *Introduction to Scientific Computing and Data Analysis (Texts in Computational Science and Engineering)*, Springer International Publishing Switzerland, 2016.

[23] Lowry, T., Allen, M.B. & Shive, P.N., *Singularity Removal: A Refinement of Resistivity Modeling Techniques*, Geophysics, **54**(6), 766-774, 1989.

[24] Zhao, S. & Yedlin, M.J., *Some Refinements on the Finite-Difference Method for 3-D DC Resistivity Modeling*, Geophysics, **61**(5), 1301-1307, 1996.

[25] Pan, K. & Tang, J., *Advance 2.5-D and 3-D DC Resistivity Modelling Using an Extrapolation Cascadic Multigrid Method*, Geophys. J. Int., **197**, pp. 1459-1470, 2014.

[26] Reynolds, J.M., *An Introduction to Applied and Environment Geophysics*, John Willey & Sons, pp. 418-488, 1997.